AIAA Aviation
June 22-26, 2015, Dallas, TX
33rd AIAA Applied Aerodynamics Conference

Delayed Detached Eddy Simulation of Projectile Flows

Jiaye Gan *, Ge-Cheng Zha†
Dept. of Mechanical and Aerospace Engineering
University of Miami
Coral Gables, Florida 33124
E-mail: gzha@miami.edu

Abstract

This paper conducts Delayed-Detached Eddy Simulation (DDES) of a guided projectile base flows. The inviscid fluxes are evaluated by the 5th order weighted essentially non-oscillatory (WENO) scheme with the low diffusion E-CUSP approximate Riemann solver and the viscous fluxes are calculated by second order central differencing. Time marching is performed with the second-order dual time stepping scheme and implicit unfactored Gauss-Seidel line iteration method in order to achieve high convergence rate. The accuracy of the DDES is validated with the force and moment experimental data. The DDES predicts the time averaged drag more accurately than the URANS and RANS. The primary difference of the drag prediction between the DDES and URANS is the pressure drag prediction in the base region. The DDES is demonstrated to be superior to the URANS for the projectile flow prediction due to more accurate base large vortex structures and pressure simulation.

1 Introduction

Accurate prediction of force and moment of projectiles is very challenge since Reynolds-averaged Navier-Strokes (RANS) equations cannot predict vortical base flows accurately. The weakness of RANS motivates the large eddy simulation(LES), which directly resolves large eddy structures and models the small eddies that are more isotropic. LES requires significant more computational time than RANS. The excessive CPU requirement, particularly in the near-wall regions, leads to the development of hybrid models to combine the best aspects of RANS and LES methodologies. An example of a hybrid technique is the detached-eddy simulation (DES) approach[1]. This model attempts to treat the near-wall regions in a RANS-like manner, and treat the rest of the flow in an LES-like manner. DES appears to be a suitable compromise between the physical models of turbulence and CPU efficiency. However, with the spread of successful DES applications [2, 3, 4], a defect of the first generation DES model(DES97) was also exposed. DES may behave unfavorably in the regions of thick boundary layers and shallow separation regions due to the grid spacing dependence[5]. Delayed detached-eddy simulation (DDES) by Spalart[5] is an improved version of the original DES97 model to overcome the Model Stress Depletion(MSD) problem. In the framework of DDES, a blending function similar to the one used by Menter and Kuntz [6] for the SST model is introduced. It limits the DES length scale to ensure the transition of RANS to LES be independent of grid spacing. The DDES model has demonstrated excellent agreement with experiment and a significant improvement over the DES97 for the tested cases presented by previous studies[5, 7].

* Graduate Student, AIAA Member
† Professor, AIAA Associate Fellow

Many efforts have been made to simulate the aerodynamic force and moment of projectiles with various degree of success. Weinacht et al[8] use the Parabolic Navier-Stokes(PNS) method to calculate pitch damping from a coning motion for bodies of revolution at supersonic velocities. The predicted pitch-damping force and moment coefficients have excellent agreement with the experiment. However, the friction force along streamwise direction and bases drag can not be predicted accurately with PNS method. DeSpiri et al [9] predict the aerodynamic coefficients of a spinned projectile in the subsonic and transonic flow regimes with detached eddy simulation. The highest deviation of the predicted roll damping is about 15% from the experiment. Sahu et al[10] used coupled CFD/rigid body dynamics (RBD) techniques to compute the aerodynamic forces and moments of the finned projectile. It was shown that the flight trajectory can be calculated fiarly well with the coupled method.

The objective of this paper is two folds: 1)perform advanced DDES of projectile flow to accurately predict the aerodynamic moments and forces; 2)Investigate and understand the flow physics to guide high performance projectile design.

2 Numerical Methodology

The DDES of Spalart[5] is employed with the recently developed low diffusion E-CUSP scheme[11] and the 5th order WENO scheme for the inviscid fluxes and 2nd order central differencing scheme for viscous terms. An implicit unfactored Gauss-Seidel line iteration is used to achieve high convergence rate. The high-scalability numerical technique is applied to save wall clock time[12].

Governing Equations. The governing equations for the flow field computation are the spatially filtered 3D time accurate compressible Navier-Stokes equations in generalized coordinates(ξ, η, ζ) and can be expressed as the following conservative form:

$$\frac{\partial \mathbf{Q}}{\partial t} + \frac{\partial \mathbf{E}}{\partial \xi} + \frac{\partial \mathbf{F}}{\partial \eta} + \frac{\partial \mathbf{G}}{\partial \zeta} = \frac{1}{Re}\left(\frac{\partial \mathbf{E}_v}{\partial \xi} + \frac{\partial \mathbf{F}_v}{\partial \eta} + \frac{\partial \mathbf{G}_v}{\partial \zeta}\right) + \mathbf{S} \tag{1}$$

where Re is the Reynolds number. Delayed detached eddy simulation(DDES) turbulence model introduced by Sparlat et al.[5] is used to close the system of equations. The equations are nondimenisonalized based on the blade chord length L_∞, upstream characteristic density ρ_∞ and velocity U_∞.

The conservative variable vector $\mathbf{Q}$, the inviscid flux vectors $\mathbf{E}$, $\mathbf{F}$, $\mathbf{G}$, the viscous fluxes $\mathbf{E_v}$, $\mathbf{F_v}$, $\mathbf{G_v}$ and the source term vector $\mathbf{S}$ are expressed as

$$\mathbf{Q} = \frac{1}{J}\begin{pmatrix} \bar{\rho} \\ \bar{\rho}\tilde{u} \\ \bar{\rho}\tilde{v} \\ \bar{\rho}\tilde{w} \\ \bar{\rho}\tilde{e} \\ \bar{\rho}\tilde{\nu}_t \end{pmatrix}, \mathbf{E} = \begin{pmatrix} \bar{\rho}U \\ \bar{\rho}\tilde{u}U + l_x\bar{p} \\ \bar{\rho}\tilde{v}U + l_y\bar{p} \\ \bar{\rho}\tilde{w}U + l_z\bar{p} \\ (\bar{\rho}\tilde{e} + \bar{p})U - l_t\bar{p} \\ \bar{\rho}\tilde{\nu}_t U \end{pmatrix} \tag{2}$$

$$\mathbf{F} = \begin{pmatrix} \bar{\rho}V \\ \bar{\rho}\tilde{u}V + m_x\bar{p} \\ \bar{\rho}\tilde{v}V + m_y\bar{p} \\ \bar{\rho}\tilde{w}V + m_z\bar{p} \\ (\bar{\rho}\tilde{e} + \bar{p})V - m_t\bar{p} \\ \bar{\rho}\tilde{\nu}_t V \end{pmatrix} \tag{3}$$

$$\mathbf{G} = \begin{pmatrix} \bar{\rho}W \\ \bar{\rho}\tilde{u}W + n_x\bar{p} \\ \bar{\rho}\tilde{v}W + n_y\bar{p} \\ \bar{\rho}\tilde{w}W + n_z\bar{p} \\ (\bar{\rho}\tilde{e} + \bar{p})\,W - n_t\bar{p} \\ \bar{\rho}\tilde{\nu}_t W \end{pmatrix} \tag{4}$$

$$\mathbf{E_v} = \begin{pmatrix} 0 \\ l_k\bar{\tau}_{xk} \\ l_k\bar{\tau}_{yk} \\ l_k\bar{\tau}_{zk} \\ l_k\left(\tilde{u}_i\bar{\tau}_{ki} - \bar{q}_k\right) \\ \frac{\bar{\rho}}{\sigma}\left(\tilde{\nu} + \tilde{\nu}_t\right)\left(\mathbf{l} \bullet \nabla\tilde{\nu}_t\right) \end{pmatrix} \tag{5}$$

$$\mathbf{F_v} = \begin{pmatrix} 0 \\ m_k\bar{\tau}u_{xk} \\ m_k\bar{\tau}_{yk} \\ m_k\bar{\tau}u_{zk} \\ m_k\left(\tilde{u}_i\bar{\tau}_{ki} - \bar{q}_k\right) \\ \frac{\bar{\rho}}{\sigma}\left(\tilde{\nu} + \tilde{\nu}_t\right)\left(\mathbf{m} \bullet \nabla\tilde{\nu}_t\right) \end{pmatrix} \tag{6}$$

$$\mathbf{G_v} = \begin{pmatrix} 0 \\ n_k\bar{\tau}_{xk} \\ n_k\bar{\tau}_{yk} \\ n_k\bar{\tau}_{zk} \\ n_k\left(\tilde{u}_i\bar{\tau}_{ki} - \bar{q}_k\right) \\ \frac{\bar{\rho}}{\sigma}\left(\tilde{\nu} + \tilde{\nu}_t\right)\left(\mathbf{n} \bullet \nabla\tilde{\nu}_t\right) \end{pmatrix} \tag{7}$$

$$\mathbf{S} = \frac{1}{J}\begin{pmatrix} 0 \\ 0 \\ 0 \\ 0 \\ 0 \\ S_\nu \end{pmatrix} \tag{8}$$

where ρ is the density, p is the static pressure, and e is the total energy per unit mass. The over bar denotes a regular filtered variable, and the tilde is used to denote the Favre filtered variable. U, V and W are the contravariant velocities in ξ, η, ζ directions, and defined as follows.

$$U = l_t + \mathbf{l} \bullet \mathbf{V} = l_t + l_x\tilde{u} + l_y\tilde{v} + l_z\tilde{w} \tag{9}$$

$$V = m_t + \mathbf{m} \bullet \mathbf{V} = m_t + m_x\tilde{u} + m_y\tilde{v} + m_z\tilde{w} \tag{10}$$

$$W = n_t + \mathbf{n} \bullet \mathbf{V} = n_t + n_x\tilde{u} + n_y\tilde{v} + n_z\tilde{w} \tag{11}$$

where l_t, m_t and n_t are the components of the interface contravariant velocity of the control volume in ξ, η and ζ directions respectively. $\mathbf{l}$, $\mathbf{m}$ and $\mathbf{n}$ denote the normal vectors located at the centers of ξ, η and ζ interfaces of the control volume with their magnitudes equal to the surface areas and pointing to the directions of increasing ξ, η and ζ. J is the Jacobian of the transformation. The source term S_ν in eq. (8),

is given by

$$\begin{array}{c} S_\nu = \bar{\rho} C_{b1} \left(1 - f_{t2}\right) \tilde{S} \tilde{\nu}_t \\ + \frac{1}{Re} \left[-\bar{\rho} \left(C_{w1} f_w - \frac{C_{b1}}{\kappa^2} f_{t2} \right) \left(\frac{\tilde{\nu}_t}{d} \right)^2 \right. \\ \left. + \frac{\bar{\rho}}{\sigma} C_{b2} \left(\nabla \tilde{\nu}_t \right)^2 - \frac{1}{\sigma} \left(\tilde{\nu} + \tilde{\nu}_t \right) \nabla \tilde{\nu}_t \bullet \nabla \bar{\rho} \right] \\ + Re \left[\bar{\rho} f_{t1} \left(\Delta q \right)^2 \right] \end{array} \tag{12}$$

where

$$\tilde{\nu_t} = \tilde{\nu} f_{v1} \qquad \chi = \frac{\tilde{\nu}}{\nu} \tag{13}$$

$$f_{v1} = \frac{\chi^3}{\chi^3 + c_{v1}^3} \qquad f_{v2} = 1 - \frac{\chi}{1 + \chi f_{v1}} \tag{14}$$

$$f_{t1} = C_{t1} g_t exp \left[-C_{t2} \frac{\omega_t^2}{\Delta U^2} \left(d^2 + g_t^2 d_t^2 \right) \right] \tag{15}$$

$$f_{t2} = C_{t3} exp \left(-C_{t4} \chi^2 \right) \qquad f_w = g(\frac{1 + c_{w3}^6}{g^6 + c_{w3}^6})^{1/6} \tag{16}$$

$$g = r + c_{w2}(r^6 - r) \qquad g_t = min \left(0.1, \frac{\Delta q}{\omega_t \Delta x_t} \right) \tag{17}$$

$$\tilde{S} = S + \frac{\tilde{\nu}}{k^2 d^2} f_{v2} \tag{18}$$

$$r = \frac{\tilde{\nu}}{\tilde{S} k^2 d^2} \tag{19}$$

where, ω_t is the wall vorticity at the wall boundary layer trip location, d is the distance to the closest wall, d_t is the distance of the field point to the trip location, Δq is the difference of the velocities between the field point and the trip location, Δx_t is the grid spacing along the wall at the trip location. The values of the coefficients are: $c_{b1} = 0.1355, c_{b2} = 0.622, \sigma = \frac{2}{3}, c_{w1} = \frac{c_{b1}}{k^2} + (1 + c_{b2})/\sigma, c_{w2} = 0.3, c_{w3} = 2, k = 0.41, c_{v1} = 7.1, c_{t1} = 1.0, c_{t2} = 2.0, c_{t3} = 1.1, c_{t4} = 2.0$.

The shear stress $\bar{\tau}_{ik}$ and total heat flux $\bar{q}_k$ in Cartesian coordinates is given by

$$\bar{\tau}_{ik} = \left(\tilde{\mu} + \tilde{\mu}_t \right) \left[\left(\frac{\partial \tilde{u}_i}{\partial x_k} + \frac{\partial \tilde{u}_k}{\partial x_i} \right) - \frac{2}{3} \delta_{ik} \frac{\partial \tilde{u}_j}{\partial x_j} \right] \tag{20}$$

$$\bar{q}_k = - \left(\frac{\tilde{\mu}}{Pr} + \frac{\tilde{\mu}_t}{Pr_t} \right) \frac{\partial \tilde{T}}{\partial x_k} \tag{21}$$

where $\tilde{\mu}$ is from Sutherland's law, and $\tilde{\mu_t}$ is determined by the S-A model. Coefficients in Eq.(8) given by reference[13] are used. The above equations are in the tensor form, where the subscripts i, k represents the coordinates x, y, z and the Einstein summation convention is used. Eq.(20) and (21) are transformed to the generalized coordinate system in computation.

To overcome grid induced separation problem, the DDES model by Sparlat et al.[5] switches the subgrid scale formulation in S-A model as follows

$$\tilde{d} = d - f_d max(0, d - C_{DES} \Delta) \tag{22}$$

where

$$f_d = 1 - tanh([8 r_d]^3) \tag{23}$$

$$r_d = \frac{\nu_t + \nu}{(U_{i,j}U_{i,j})^{0.5}k^2d^2} \tag{24}$$

where Δ is the largest spacing of the grid cell in all the directions. Within the boundary layer close to walls, $\tilde{d} = d$, and away from the boundary layer, $\tilde{d} = d - f_d max(0, d - C_{DES}\Delta)$ is most of the cases. This mechanism enables DDES to behave as a RANS model in the near-wall region, and the LES away from the walls. This modification in $\tilde{d}$ reduces the grey transition area between RANS and LES. The coefficient $C_{DES} = 0.65$ is used as set in the homogeneous turbulence[14]. The Pr_t may take the value of 0.9 within the boundary layer for RANS mode and 0.5 for LES mode away from the wall surface.

The equation of state as a constitutive equation relating density to pressure and temperature is defined as:

$$\bar{\rho}\tilde{e} = \frac{\bar{p}}{(\gamma - 1)} + \frac{1}{2}\bar{\rho}(\tilde{u}^2 + \tilde{v}^2 + \tilde{w}^2) \tag{25}$$

where γ is the ratio of specific heats. For simplicity, all the bar and tilde in above equations will be dropped in the rest of this paper.

Time Marching Scheme. The time dependent governing equation (1) is solved with the dual time stepping method suggested by Jameson[15]. A pseudo temporal term $\frac{\partial Q}{\partial \tau}$ is added to the governing Eq. (1). This term vanishes at the end of each physical time step, and has no influence on the accuracy of the solution. An implicit pseudo time marching scheme using Gauss-Seidel line relaxation is employed to achieve high convergence rate instead of using the explicit scheme. The physical temporal term is discretized implicitly using a three point, backward differencing as the following:

$$\frac{\partial \mathbf{Q}}{\partial t} = \frac{\mathbf{3Q^{n+1} - 4Q^n + Q^{n-1}}}{2\Delta t} \tag{26}$$

where $n-1$, n and $n+1$ are three sequential time levels, which have a time interval of Δt. The first-order Euler scheme is used to discretize the pseudo temporal term. The semi-discretized equations of the governing equations are given as the following:

$$\begin{aligned}\left[\left(\tfrac{1}{\Delta\tau} + \tfrac{1.5}{\Delta t}\right) I - \left(\tfrac{\partial R}{\partial \mathbf{Q}}\right)^{n+1,m}\right] \delta\mathbf{Q^{n+1,m+1}} \\ = R^{n+1,m} - \tfrac{\mathbf{3Q^{n+1,m} - 4Q^n + Q^{n-1}}}{2\Delta t}\end{aligned} \tag{27}$$

where the $\Delta\tau$ is the pseudo time step, and R means the net flux going through the control volume, given by

$$R = \tfrac{1}{V}\int_s [(\mathbf{E_v} - \mathbf{E}) + (\mathbf{F_v} - \mathbf{F}) + (\mathbf{G_v} - \mathbf{G})] \cdot d\mathbf{s} \tag{28}$$

where V is the volume of the control volume and s is the control volume surface area vector.

Approximate Riemann Solver. An accurate Riemann solver is necessary to calculate the interface fluxes with shock discontinuities. The Low Diffusion E-CUSP (LDE) Scheme suggested by Zha et al [11] is used to evaluate the inviscid fluxes with the 5th order WENO scheme[16]. The variables are extrapolated to the cell interface as left(L) and right(R) values using the values on neighboring cells, then the inviscid fluxes are reconstructed based on these extrapolated variables. The basic idea of the LDE scheme is to split the inviscid flux into the convective flux E^c and the pressure flux E^p. With an extra equation from the S-A model for DDES, the splitting using the LDE scheme is basically the same as the original scheme for the Euler equation. This is an advantage over the Roe scheme[17], for which the eigenvectors need to be derived when any extra equation is added to the governing equations. In [18], the LDE scheme is shown to be more efficient than the Roe scheme when the S-A one equation turbulence model is coupled.

The 5th Order WENO Scheme. The interface flux, $E_{i+\frac{1}{2}} = E(Q_L, Q_R)$, is evaluated by determining the conservative variables Q_L and Q_R using fifth-order WENO scheme[16]. For example,

$$(Q_L)_{i+\frac{1}{2}} = \omega_0 q_0 + \omega_1 q_1 + \omega_2 q_2 \tag{29}$$

where

$$\begin{array}{l} q_0 = \frac{1}{3}Q_{i-2} - \frac{7}{6}Q_{i-1} + \frac{11}{6}Q_i \\ q_1 = -\frac{1}{6}Q_{i-1} + \frac{5}{6}Q_i + \frac{1}{3}Q_{i+1} \\ q_2 = \frac{1}{3}Q_i + \frac{5}{6}Q_{i+1} - \frac{1}{6}Q_{i+2} \end{array} \tag{30}$$

$$\omega_k = \frac{\alpha_k}{\alpha_0 + \ldots + \alpha_{r-1}} \tag{31}$$

$$\begin{array}{l} \alpha_k = \frac{C_k}{\epsilon + IS_k},\ k = 0, \ldots, r-1 \\ C_0 = 0.1,\ C_1 = 0.6,\ C_2 = 0.3 \\ IS_0 = \frac{13}{12}\left(Q_{i-2} - 2Q_{i-1} + Q_i\right)^2 + \\ \qquad \frac{1}{4}\left(Q_{i-2} - 4Q_{i-1} + 3Q_i\right)^2 \\ IS_1 = \frac{13}{12}\left(Q_{i-1} - 2Q_i + Q_{i+1}\right)^2 + \frac{1}{4}\left(Q_{i-1} - Q_{i+1}\right)^2 \\ IS_2 = \frac{13}{12}\left(Q_i - 2Q_{i+1} + Q_{i+2}\right)^2 + \\ \qquad \frac{1}{4}\left(3Q_i - 4Q_{i+1} + Q_{i+2}\right)^2 \end{array} \tag{32}$$

where, ϵ is originally introduced to avoid the denominator becoming zero and is supposed to be a very small number. In [16], it is observed that IS_k will oscillate if ϵ is too small and also shift the weights away from the optimal values in the smooth region. The higher the ϵ values, the closer the weights approach the optimal values, C_k, which will give the symmetric evaluation of the interface flux with minimum numerical dissipation. When there are shocks in the flow field, ϵ can not be too large to maintain the sensitivity to shocks. In [16], $\epsilon = 10^{-2}$ is recommended for the transonic flow with shock waves. In this paper, since there is no shock in the flow, the $\epsilon = 0.3$ is used.

3 Mesh and boundary condition

The projectile calculated in this paper is an cone-cylinder-finned configuration as shown in Fig. 1. The length of the projectile model is 12.5in and the diameter is 1.25in. The cone nose is 3.5 in long and the after-body length is 9 in. Four fins are located at the end of the projectile. Each fin has the dimension of 1.25in in long, 1.25in in height and 1in in thickness. The Mach number is 0.752 and Reynolds number is 400000.

The computational mesh for the projectile model is in a O-type shape as shown in Fig. 2. Two different domain sizes of computational model are tested for considering the effect of the far-field boundary on the results. One model is 3 times body length away from the model in all the three directions. The other mesh has a bigger domain, which uses a large domain mesh surrounding a smaller mesh domain. The final size of the computational domain is about 40 times of the body length of the projectile in all the directions. To avoid singular point at the tip of the nose, a small tip "O-type" block is created. Fig. 2 shows a 3-D view of the full projectile mesh. The total number of grid points of the small computational domain is about 7 million with 184 blocks. The mesh size of the large domain is about 14 million with 328 blocks. Fig. 3 shows an expanded view of the grid in the small mesh. The first wall grid point spacing is at Y^+ value of about 1.0 for both the meshes. The growth rate of the grids away from the solid wall is 1.25.

The total pressure, total temperature and flow angle are specified at computational domain inlet as the boundary conditions. The static pressure at the outlet is specified to determine the freestream Mach number. In the computation, the free stream flow is kept horizontal. For a flow with an angle of attack(AoA), the mesh is rotated to create the AoA as demonstrated in Fig. 3.

4 Results and Discussion

The simulations are performed with parallel computing with about 40,000-50,000 cells in each mesh block. The calculations took about 10 hours to converge for steady simulation and 168 hours for the unsteady DDES calculation. The unsteady calculation reaches the stable solution at about 250 characteristic time. The solution residuals are reduced at least 2 orders of magnitude within each physical time step and the aerodynamic coefficients vary less than 0.1% over the last 100 time steps. The aerodynamic force coefficients are the determining factor in convergence.

To accurately predict wall friction, the mesh near the solid surface is refined. However, the quality of the mesh may decrease due to the high aspect ratio as the number of grid points is increased in the boundary layer. To have a suitable mesh density with acceptable CPU time and numerical accuracy, three different grid distributions are tested for grid convergence. The first mesh(Mesh1) is to make sure y^+=1 on every solid wall surface, including the leading edge, the tip surfaces of the fins and solid surface at the leading edge of the nose. The second one(Mesh2) is to keep the same grid distribution as mesh1, except neglecting the effect of small walls, including the surfaces at the leading edge and the tips of the fins, and the surface at the leading edge of the nose. Coarse grid distribution are used on those small wall surfaces and wall function boundary conditions are employed for Mesh2. To study the effect of y^+ on the forces calculation, a third computational mesh (Mesh3) with y^+ value equal to 6 is tested. All cases are run at AoA=0° with RANS model. The Mach number using in the grid convergence test is 0.677. The computed axial forces with different meshes are presented in Table 1. We can see that the predicted force and moment from Mesh1 and Mesh2 are almost the same and closer to experiment data than that of Mesh3. The computed y^+ of Mesh2 and Mesh3 at wall surface are shown in Fig. 4. It can be seen that y^+=1.0 around the cylinder body are achieved in Mesh2. Therefore, Mesh2 is used in the unsteady DDES simulation.

To reduce the uncertainty in the drag prediction, two different ways of wall shear stress calculation are developed. Method 1 is based on the velocity gradient near the wall, in which the tangential velocity and the distance of the first cell center away from the wall are calculated. The other method (Method 2) extracts the shear stress directly from the viscous term of the Navier-Stokes equations. The results are shown in 5. It is shown that both results are in excellent agreement.

The time history of CA, CN, CM_pitching and CM_roll at AoA=0° and M=0.752 are shown in Fig. 6. The results of DDES method are compared with those of URANS. Both simulations are started from the same RANS results. The predicted drag of DDES agree better with the experiment than the URANS. The difference of the drag prediction by DDES and URANS in the subsonic regime indicates that the unsteady wake flow impacts the upstream side forces. The roll moment from the URANS follows the same trends as that of DDES.

The DDES force and moment convergence history of CA, CN, CM_pitching and CM_roll at AoA=4° and M=0.752 are shown in Fig. 7 and Fig. 8. The URANS is used for the first 2000 time steps and the calculation is switched to DDES. Fig. 8 shows that there are discontinuities in the convergence histories when the calculation is switched from URANS to DDES.

The results of RANS, URANS and DDES at AoA=0° and M=0.752 are summarized in Table 2. From the table, DDES significantly reduce the axial force prediction error to about 4.5%, URANS has an error of 12.3%, and RANS has an error of 16.6%. DDES is demonstrated to have the best accuracy among the three methods. The URANS gives more accurate results than the steady state RANS because the vortex vortex shedding in the wake region is unsteady. All three methods have excellent agreement in predicting the rolling moment. The predicted normal force and pitching moment are close to zero at AoA=0° as the experiment since the geometry is mostly axi-symmetric except the fins that generate circumferential force.

The comparisons of different methods at AoA=4° and M=0.752 are shown in Table 3. The axial force predicted by DDES has an error of 3.9% compared with the experiment, significantly more accurate than that predicted by URANS with an error of 12%. For the nomal forces, the URANS and DDES have the deviation about 10.0% and 8.7% respectively. The DDES is again more accurate than the URANS even

though the deviation is greater than the axial force.

Table 4 and Table 5 present the the breakdowns of the normal and axial forces of each component including the projectile main body, the base surface, and the fins. In the table, C_{Lp} is the lift contributed by pressure, C_{Lv} is the lift contributed by viscous shear stress lift, C_{Dp} is the drag contributed by pressure and C_{Dv} is the drag contributed by the viscous shear stresses. The predicted friction drags are almost the same between the URANS and DDES for both the case of at AoA=0° or AoA=4°. The reason is that within the wall boundary layer, URANS is also used by DDES. For the predicted pressure drag, URANS and DDES are quite different. At AoA=0°, C_{Dp} predicted by URANS is about 10% greater than that of DDES. At AoA=4°, it is about 9.5% larger. The pressure value at the base redicted by DDES is about 4% greater than that of URANS, which results in a smaller overall drag since the predicted drag of the main body are about the same. Drag contribution of the fin is about 36% of the total drag at AoA=0° and is increased to 41% at AoA=4°. The pressure drag predicted by DDES is smaller than that of URANS.

Fig. 9 shows the Mach contours obtained by URANS and DDES at AoA=0° and M=0.752 at the mid-plane. Both plots show similar flow structures over the projectile. The vortex shedding at the trailing edge of the projectile is captured as shown in Fig. 10. The flow field at AoA=4° has similar flow structure as the case at AoA=0°. Fig. 11 shows the velocity vector field behind the fins. It shows the fin tip vortices due to the lift that creates the the roll moment and cause the body to spin with magnus effect. Fig.12 illustrates instantaneous entropy contours, which indicates that the wake region suffers high loss due to the base flow. Fig 13 is the Mach number contour in the wake region for both the AoA=0° and 4°. The wakes of the fins merge with the wake of the base surface.

Fig.14 shows the instantaneous static pressure contour predicted by DDES at M=0.752. The base area has very low pressure that contributes to the base drag. Fig. 15 shows the surface pressure contours and the surface pressure distributions of the mid plane on the lower and upper side. At AoA=0°, the pressure is symmetric with no lift. The pressure decreases rapidly from leading edge to the cone-cylinder transition point due to the converging area, and then increase rapidly after that due to fast area expansion. At AoA= 4°, the pressure variation trend along the body is similar to that at AoA= 0°, but the pressures on the upper and lower side is largely different due to generating the lift. The fin surface pressure coefficients predicted by DDES at AoA=0° and 4° are shown in Fig.16 and Fig.17, respectively. At AoA=0°, the fins do not generate lift and the pressure distributions on the 4 fins are the same. At AoA=4°, the fin surface pressure are not symmetric due to the lift generation.

5 Conclusions

High order accuracy numerical algorithm is utilized to predict the force and moment of a guided projectile with DDES model. The DDES demonstrates its excellent ability to accurately simulate the vortical base flow. The predicted drag coefficients for the projectile by the DDES shows a good agreement with the experiment. For an ARDEC Projectile at M=0.752, AoA=0° and 4°, the DDES significantly reduces the axial force prediction error to about 4%, whereas the URANS has an error of 12%, and the RANS has an error of 16% to 23%. The primary difference of the drag prediction between the DDES and URANS is the pressure drag prediction in the base region. The DDES is demonstrated to be superior to the URANS for the projectile flow prediction due to more accurate base large vortex structures and pressure simulation.

6 Acknowledgment

The simulation is conducted at the high performance super-computing center of Oak Ridge National Lab, Army supercomputer center, and the center for computational sciences at the University of Miami.

References

[1] P.R. Spalart, W.H. Jou, M. Strelets, and S.R. Allmaras, "Comments on the Feasibility of LES for Wings, and on a Hybrid RANS/LES Approach." Advances in DNS/LES, 1st AFOSR Int. Conf. on DNS/LES, Greyden Press, Columbus, H., Aug. 4-8, 1997.

[2] B.Y. Wang, and G.C. Zha, " Detached Eddy Simulations of a Circular Cylinder Using a Low Diffusion E-CUSP and High-Order WENO Scheme." AIAA Paper 2008-3855, AIAA 38th Fluid Dynamics Conference, Seattle, Washington, June 23-26, 2008.

[3] S. Kapadia, and S. Roy, "Detached Eddy Simulation of Turbine Blade Cooling." AIAA Paper 2003-3632, the 36th Thermophysics Conference, Orlando, Florida, 23 - 26 June 2003.

[4] P. Spalart, "Young-Person's Guide to Detached-Eddy Simulation Grids." NASA/CR-2001-211032, 2001.

[5] P.R. Spalart, S. Deck, M. Shur, and K.D. Squires, "A New Version of Detached-Eddy Simulation, Resistant to Ambiguous Grid Densities," *Theoritical and Computational Fluid Dynamics*, vol. 20, pp. 181–195, 2006.

[6] F.R. Menter, and M. Kuntz, "Adaptation of Eddy-Viscosity Turbulence Models to Unsteady Separated Flow Behind Vehilces, *The Aerodynamics of Heavy Vehicles: Trucks, Buses and Trains, Edited by McCallen, R. Browand, F. and Ross, J.* ," *Springer, Berlin Heidelberg New York, 2004*, 2-6 Dec. 2002.

[7] Im, H.-S., and Zha, G.-C., "Delayed Detached Eddy Simulation of Airfoil Stall Flows Using High-Order Schemes," *Journal of Fluids Engineering*, vol. 136, 2014.

[8] P. Weinacht, W. B. Sturek, and L. B. Schiff, "Navier-Stokes Predictions of Pitch-Damping for Axisymmetric Shell Using Steady Coning Motion," *Journal of Spacecraft and Rockets*, vol. 34, pp. 753–761, 2013.

[9] J. DeSpirito and K. R. Heavy, "CFD Computations of Magnus Moment and Roll Damping Moment of Spinning projectile." AIAA Atmospheric Flight Mechanics Conference and Exhibit, August 16 - 19, 2004.

[10] J. Sahu and K. R. Heavy, "Parallel CFD Computations of Projectile Aerodynamics with a Flow Control Mechanism," *Computers Fluids*, 2013.

[11] G.C. Zha, Y.Q. Shen, and B.Y. Wang, "An Improved Low Diffusion E-CUSP Upwind Scheme," 2011.

[12] B.-Y. Wang, and G.-C. Zha, "A General Sub-Domain Boundary Mapping Procedure For Structured Grid CFD Parallel Computation," *AIAA Journal of Aerospace Computing, Information, and Communication*, vol. 5, pp. 425–447, 2008.

[13] P.R. Spalart, and S.R. Allmaras, "A One-equation Turbulence Model for Aerodynamic Flows." AIAA-92-0439, 1992.

[14] M. Shur, P.R. Spalart, M. Strelets, and A. Travin, "Detached-Eddy Simulation of an Airfoil at High Angle of Attack", 4th Int. Symp. Eng. Turb. Modelling and Measurements, Corsica." May 24-26, 1999.

[15] A. Jameson, "Time Dependent Calculations Using Multigrid with Applications to Unsteady Flows Past Airfoils and Wings." AIAA Paper 91-1596, 1991.

[16] Y.-Q. Shen, G.-C. Zha, and B.-Y. Wang, "Improvement of Stability and Accuracy of Implicit WENO Scheme," *AIAA Journal*, vol. 47, pp. 331–344, 2009.

[17] P. Roe, "Approximate Riemann Solvers, Parameter Vectors, and Difference Schemes," *Journal of Computational Physics*, vol. 43, pp. 357–372, 1981.

[18] B.Y. Wang, and G.C. Zha, "Comparison of a Low Diffusion E-CUSP and the Roe Scheme for RANS Calculation." AIAA Paper 2008-0596, 46th AIAA Aerospace Sciences Meeting and Exhibit, Jan. 7-10, 2008.

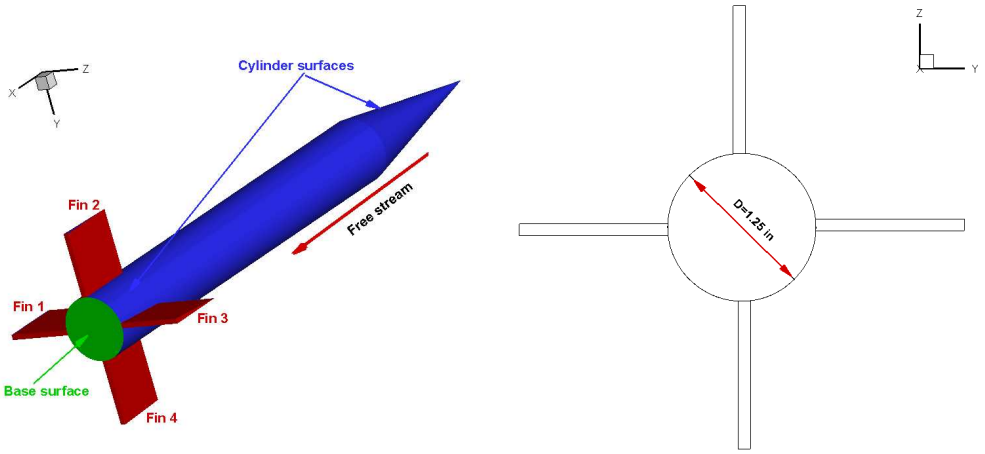

Figure 1: Geometry of projectile

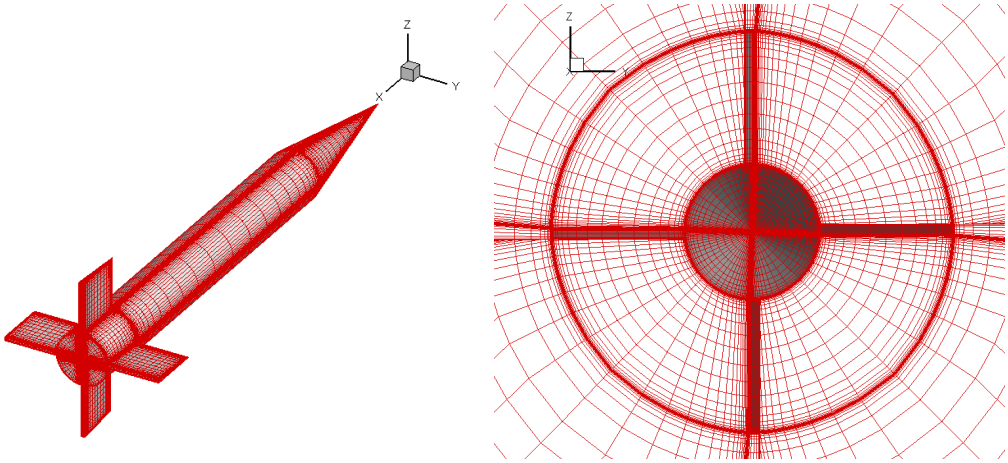

Figure 2: Surface mesh of the projectile model

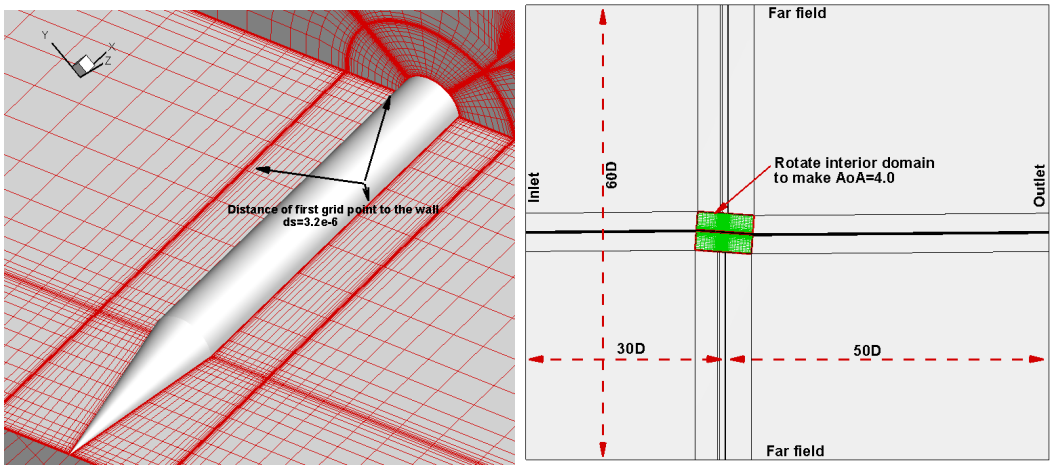

Figure 3: Iso view of the mesh

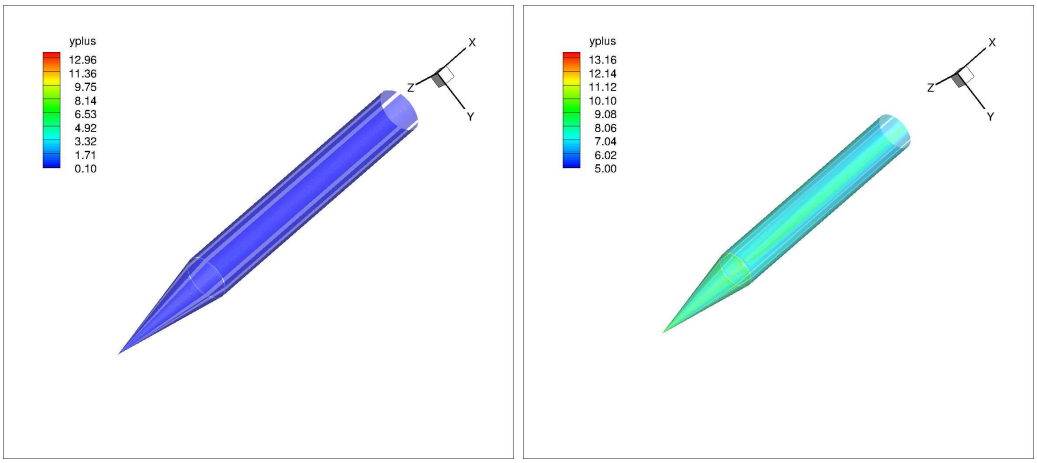

Figure 4: Boundary layer resolving mesh comparison. Left: mesh2, Right: mesh3

Table 1: Force and Moment at AoA=0°, M=0.677

Item	CA	CN	CM_pitch	CM_roll
Exp	0.521	0.000	0.000	0.331
Mesh1	0.615	0.000	0.000	0.334
Mesh2	0.618	0.000	0.000	0.334
Mesh3	0.632	0.000	0.000	0.347

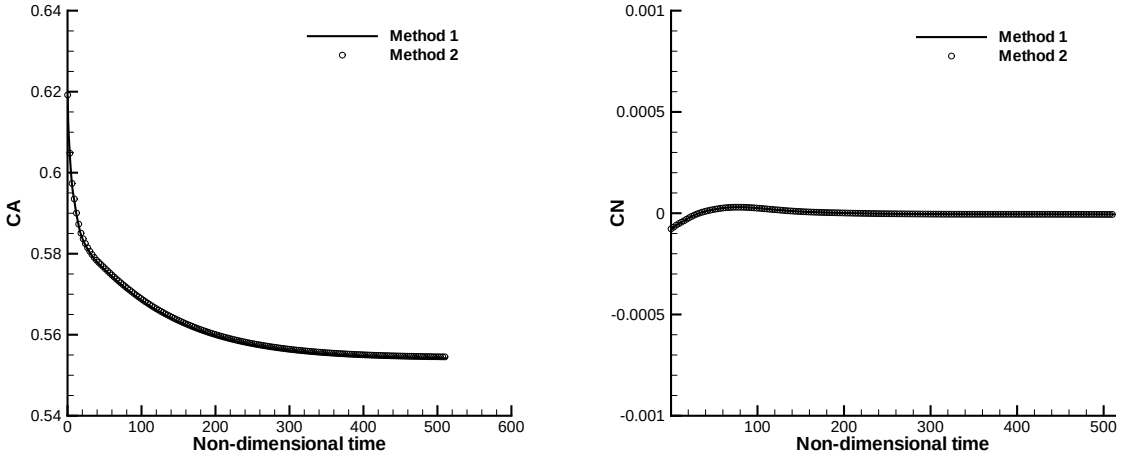

Figure 5: Force results of different calculation methods

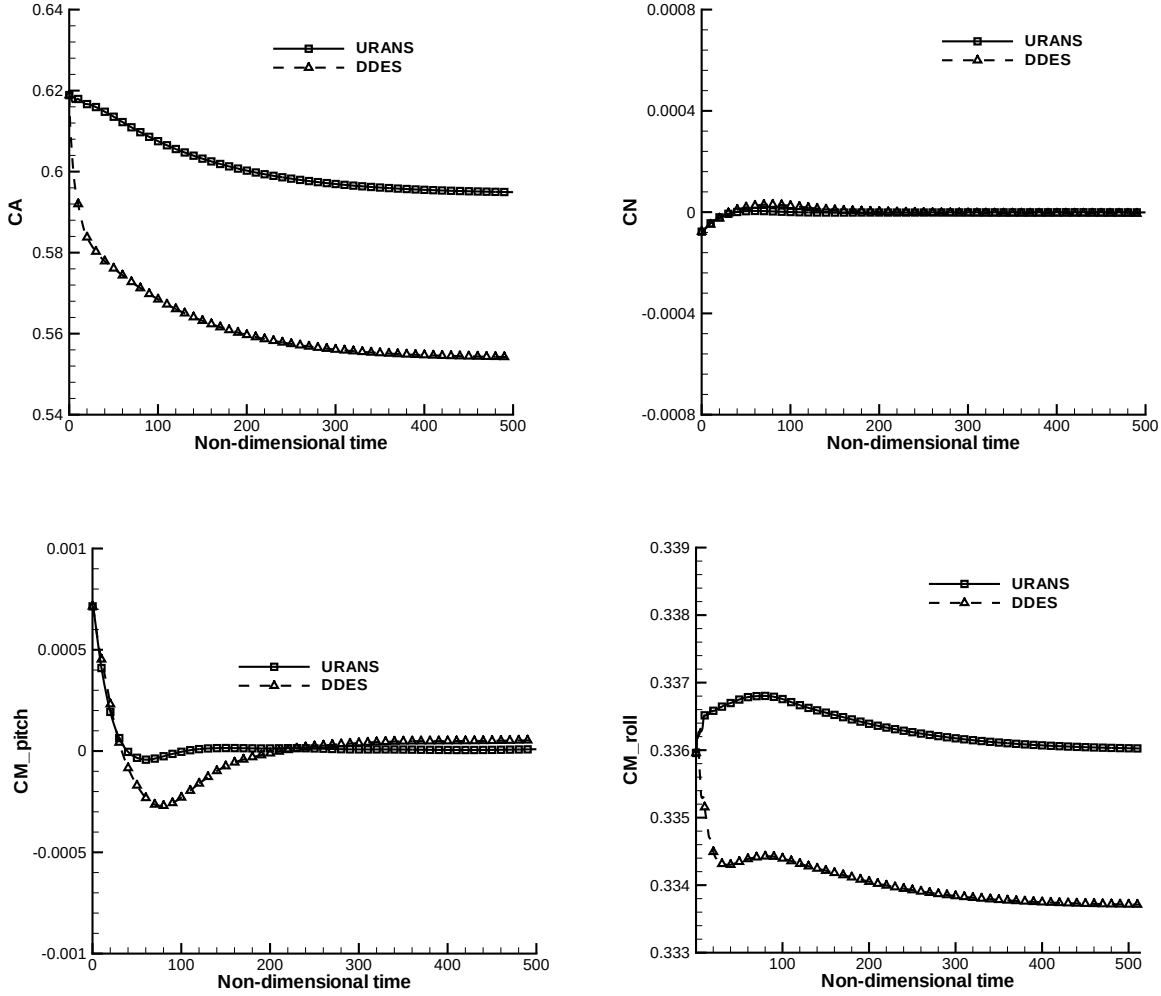

Figure 6: Coefficient of axial force(CA), normal force(CN), pitching moment(CM_pitch) and rolling moment(CM_roll) at AoA=0° and M=0.752, predicted by URANS and DDES

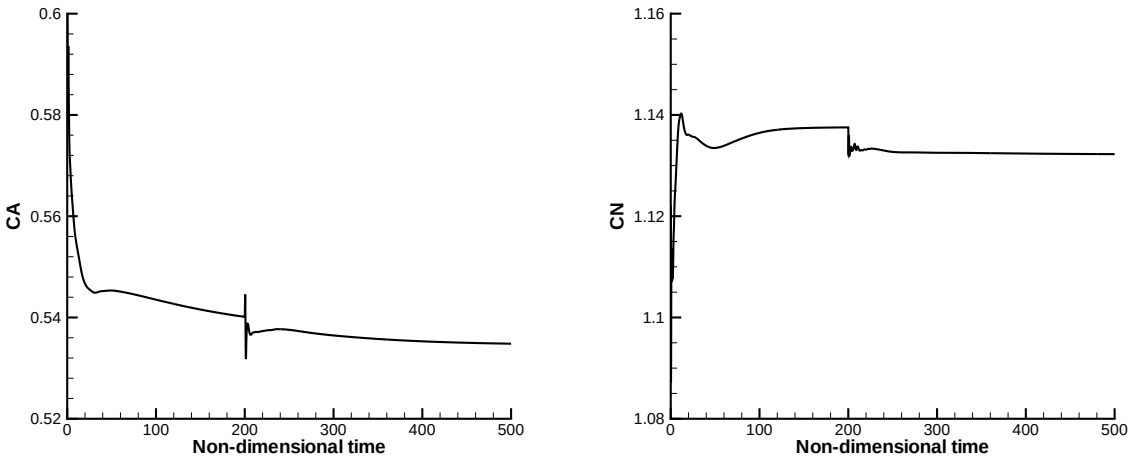

Figure 7: Force coefficient at AoA=4° and M=0.752 with DDES

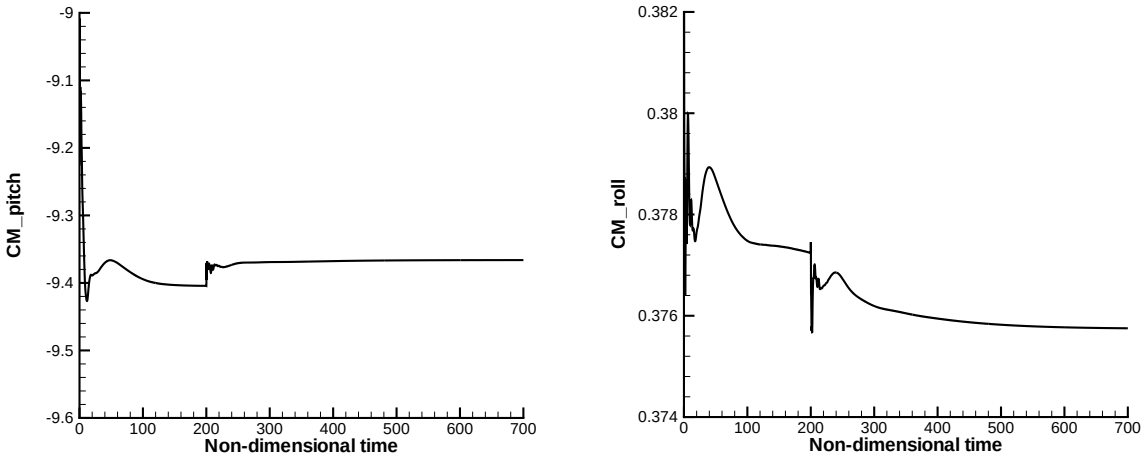

Figure 8: Moment coefficient at AoA=4° and M=0.752 with DDES

Table 2: Force and Moment at AoA=0° and M=0.752

Item	CA	error	CN	error	CM_pitch	error	CM_roll	error
Exp	0.530		0.0		0.0		0.333	
RANS	0.618	16.6%	0.0	0.0	0.0	0.0	0.336	1.0%
URANS	0.595	12.3%	0.0	0.0	0.0	0.0	0.336	1.0%
DDES	0.554	4.5%	0.0	0.0	0.0	0.0	0.334	0.3%

Table 3: Force and Moment at AoA=4.0° and M=0.752

Item	CA	error	CN	error	CM_pitch	error	CM_roll	error
Exp	0.516		1.040		-8.48		0.362	
RANS	0.635	23.1%	1.122	7.3%	-9.226	8.8%	0.384	6.1%
URANS	0.578	12.0%	1.144	10.0%	-9.464	11.6%	0.378	4.4%
DDES	0.535	3.9%	1.132	8.7%	-9.366	10.5%	0.376	3.9%

Table 4: Force contributions of different parts at AoA=0° and M=0.752

Item	Method	C_{Lp}	C_{Lv}	C_{Dp}	C_{Dv}
Cylinder	URANS	0.000	0.000	2.558	0.100
	DDES	0.000	0.000	2.558	0.100
Base	URANS	0.000	0.000	-2.268	0.000
	DDES	0.000	0.000	-2.303	0.000
Fins	URANS	0.000	0.000	0.150	0.056
	DDES	0.000	0.000	0.145	0.055

Table 5: Force contributions of different parts at AoA=4° and M=0.752

Item	Method	C_{Lp}	C_{Lv}	C_{Dp}	C_{Dv}
Cylinder	URANS	0.061	0.001	2.563	0.101
	DDES	0.058	0.001	2.562	0.101
Base	URANS	0.158	0.000	-2.264	0.000
	DDES	0.161	0.000	-2.300	0.000
Fins	URANS	0.884	-0.004	0.204	0.052
	DDES	0.876	-0.004	0.198	0.052

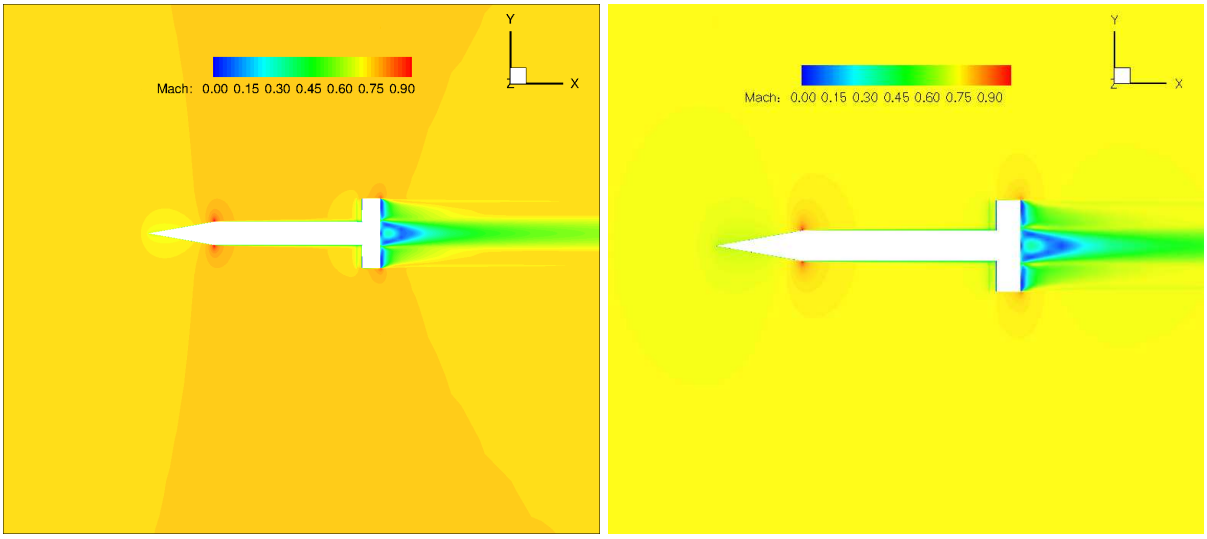

Figure 9: Instantaneous Mach number contour at AoA=0° and M=0.752, left for URANS, right for DDES

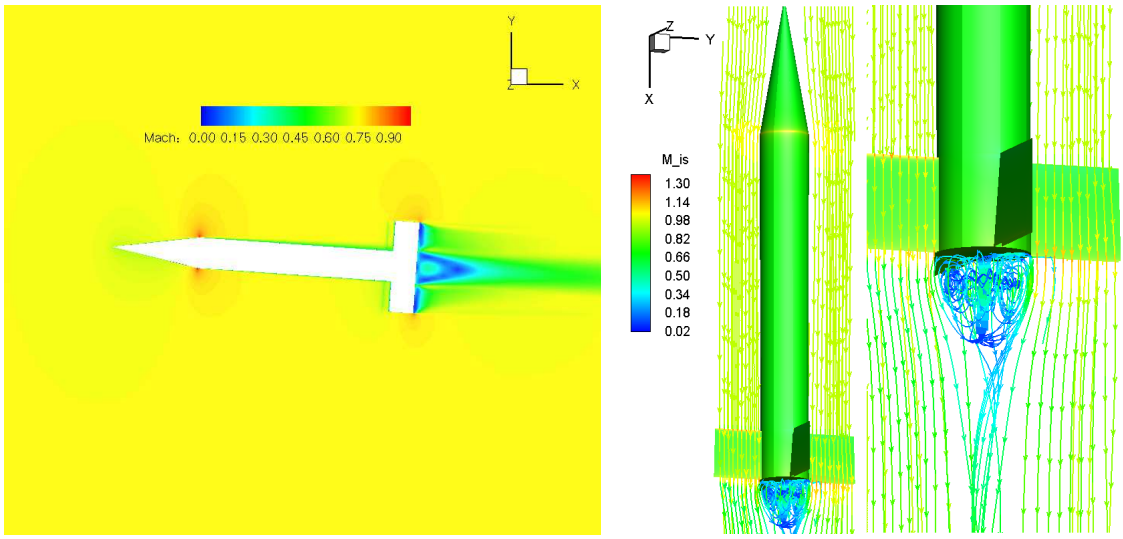

Figure 10: Flow field around the body and near the tail at AoA=4° and M=0.752, left for mach contour, right for streamline

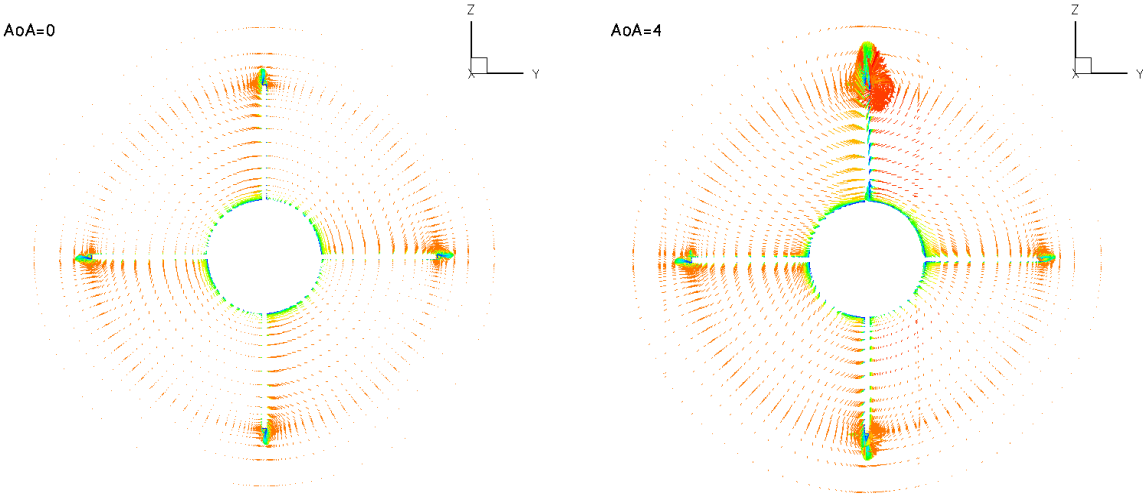

Figure 11: Vortex structure around the fin

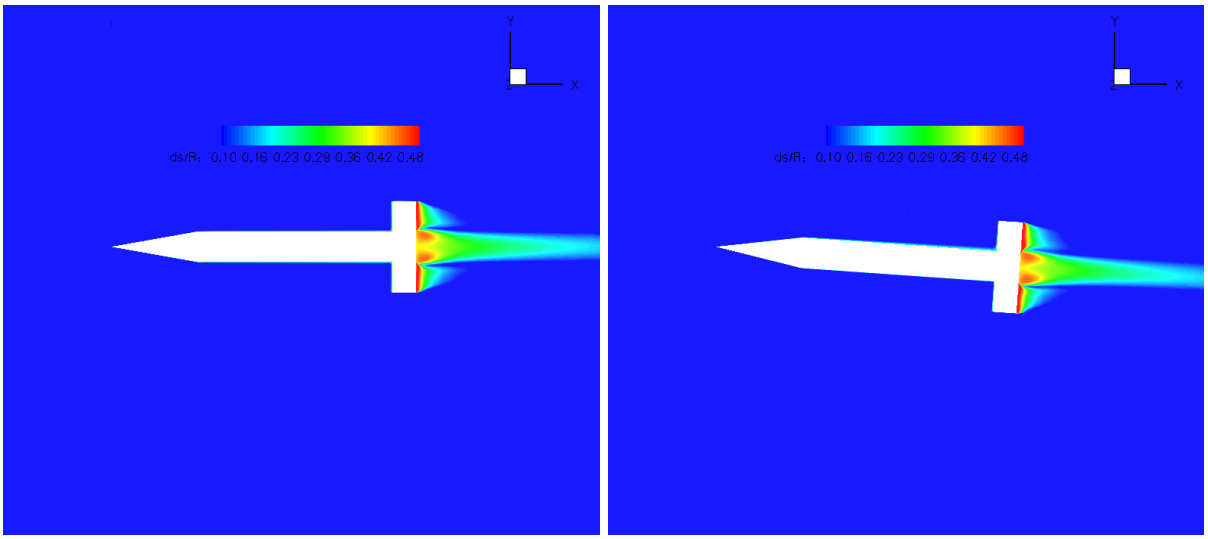

Figure 12: Entropy contour: left for AoA=0°, right for AoA=4°

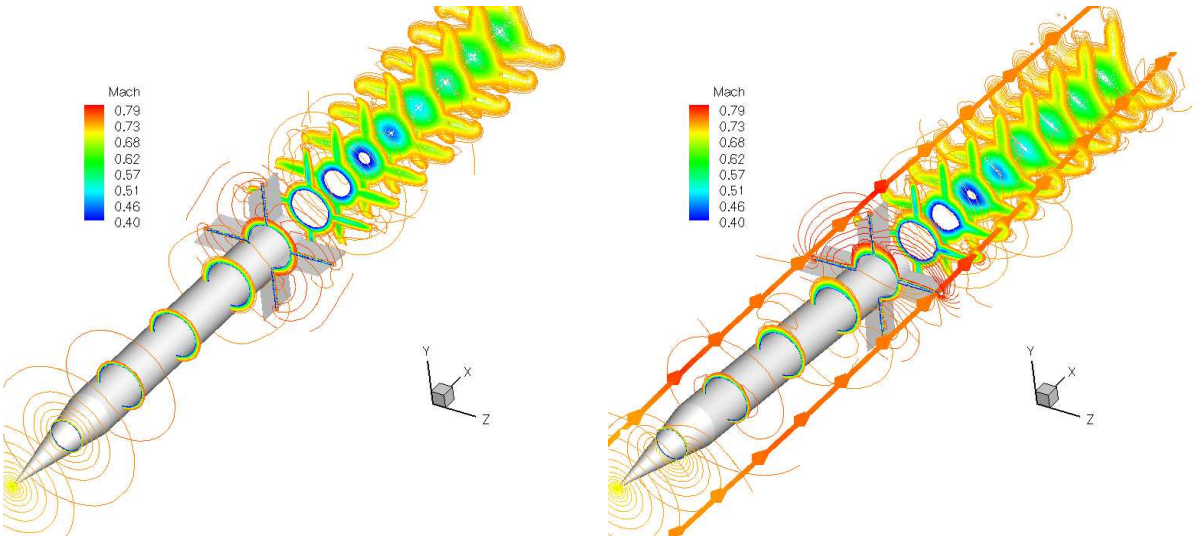

Figure 13: Mach line contours: left for AoA=0°, right for AoA=4°

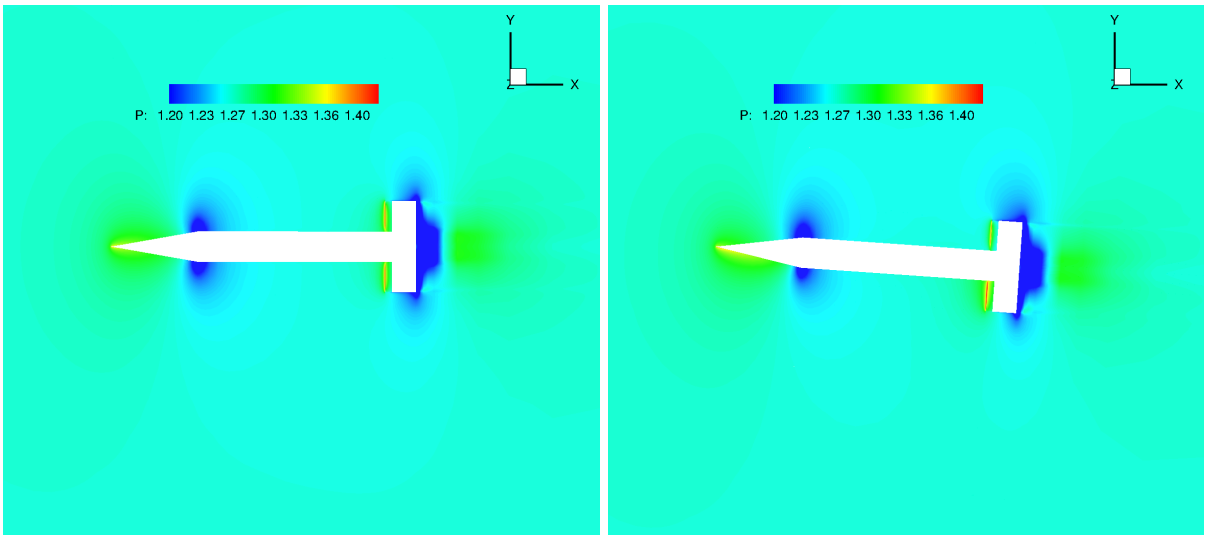

Figure 14: Static pressure contour: left for AoA=0°, right for AoA=4°

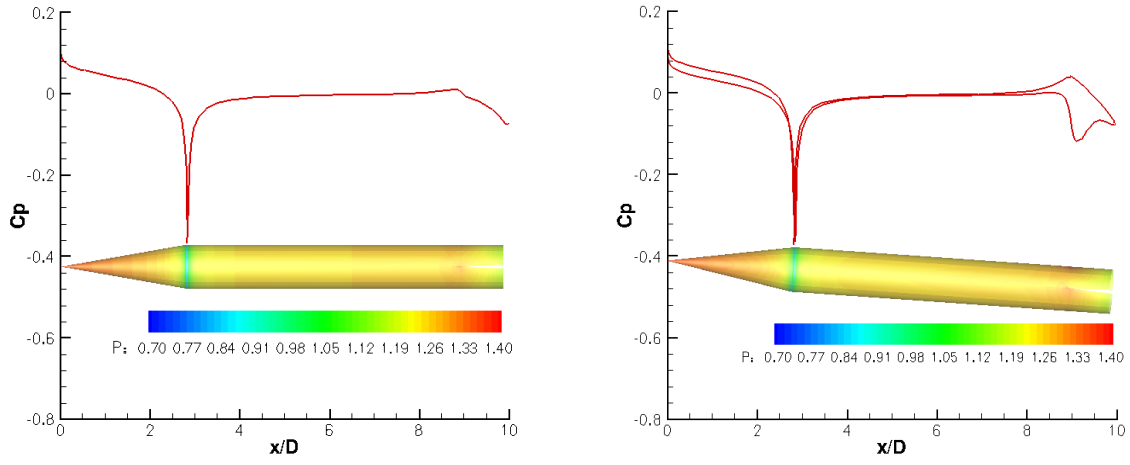

Figure 15: Computed Surface Pressure: left for AoA=0°, right for AoA=4°

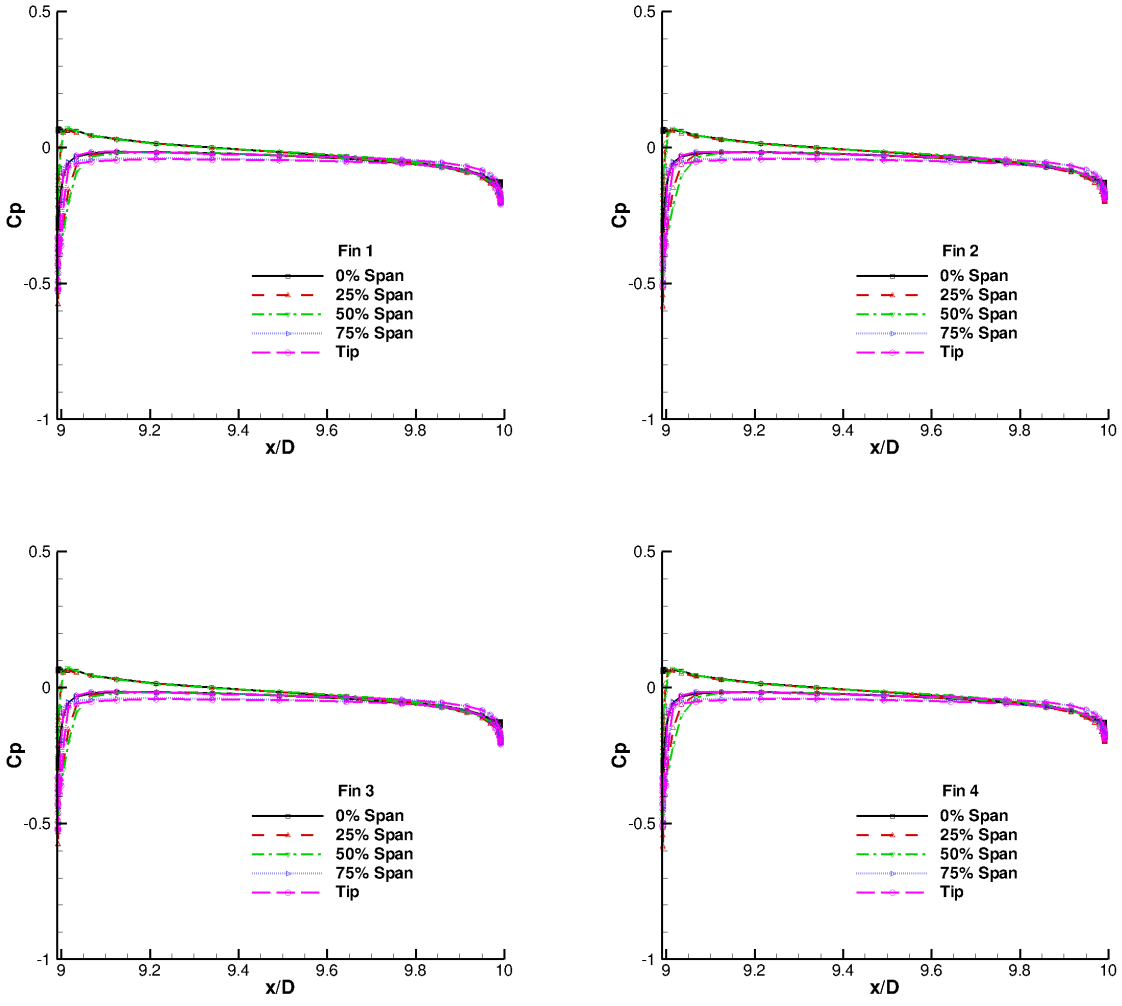

Figure 16: Computed pressure coefficient for AoA=0°

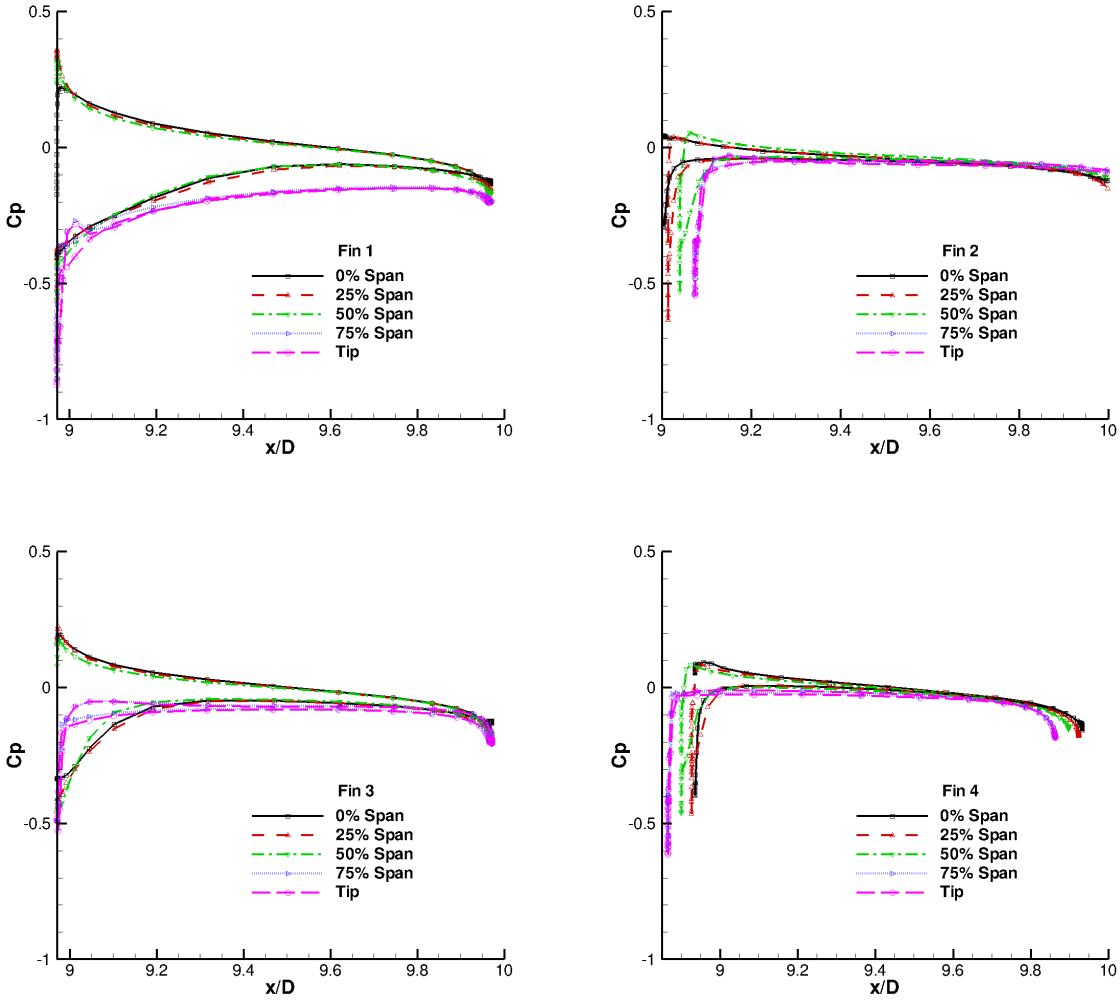

Figure 17: Computed pressure coefficient for AoA=4°